

Imaging and 3D morphological analysis of collagen fibrils

H. ALTENDORF^{*,†}, E. DECENCIÈRE[†], D. JEULIN[†],
P. DE SA PEIXOTO[‡], A. DENISET-BESSEAU[§], E. ANGELINI[¶],
G. MOSSER[‡] & M.-C. SCHANNE-KLEIN[§]

^{*}Department of Image Processing, Fraunhofer Institute of Industrial Mathematics, Kaiserslautern, Germany

[†]Centre of Mathematical Morphology, Mines Paris Tech, Fontainebleau cedex, France

[‡]Chemistry of Condensed Matter Laboratory, Université Pierre et Marie Curie, 75005 Paris, France

[§]Laboratory for Optics and Biosciences, Ecole Polytechnique, CNRS INSERM, Palaiseau, France

[¶]Department of Image and Signal Processing, Institute Telecom, Telecom ParisTech, CNRS LTCL, France

Key words. Fibre System, collagen fibrils, biopolymers, second harmonic microscopy, three-dimensional imaging, mathematical morphology, fibre segmentation.

Summary

The recent booming of multiphoton imaging of collagen fibrils by means of second harmonic generation microscopy generates the need for the development and automation of quantitative methods for image analysis. Standard approaches sequentially analyse two-dimensional (2D) slices to gain knowledge on the spatial arrangement and dimension of the fibrils, whereas the reconstructed three-dimensional (3D) image yields better information about these characteristics. In this work, a 3D analysis method is proposed for second harmonic generation images of collagen fibrils, based on a recently developed 3D fibre quantification method. This analysis uses operators from mathematical morphology. The fibril structure is scanned with a directional distance transform. Inertia moments of the directional distances yield the main fibre orientation, corresponding to the main inertia axis. The collaboration of directional distances and fibre orientation delivers a geometrical estimate of the fibre radius. The results include local maps as well as global distribution of orientation and radius of the fibrils over the 3D image. They also bring a segmentation of the image into foreground and background, as well as a classification of the foreground pixels into the preferred orientations. This accurate determination of the spatial arrangement of the fibrils within a 3D data set

will be most relevant in biomedical applications. It brings the possibility to monitor remodelling of collagen tissues upon a variety of injuries and to guide tissues engineering because biomimetic 3D organizations and density are requested for better integration of implants.

Introduction

Collagen is the main structural protein of the human body. It is mainly organized as fibrils that provide the building blocks of a variety of organs (skin, arteries, cornea, bone, tendons, etc.) (Hulmes, 2002). The spatial organization of these fibrils and their size distribution are highly specific to each organ. They determine to a large extent their biomechanical properties, which are crucial for the organ function. It is therefore of great interest to develop *in situ* and nondestructive tri-dimensional (3D) characterization methods of the collagen fibrillar network for biomedical applications. Such characterization would enable, for example, the evaluation of tissue remodelling in response to a variety of tissue injuries. Moreover, it can be used in tissue engineering to guide the synthesis of dense collagen fibrillar matrices exhibiting the same 3D organization and overall characteristics as in natural tissues. *In vitro* fundamental studies have indeed shown that cells are receptive to the mechanical properties of the matrices they are grown on, to the size or diameter of the structured holder, as well as to the porosity of the 3D matrices (Lee *et al.*, 2008; Brown & Discher, 2009). Thus, 3D characterization methods are crucial for the verification of tissue substitutes to be used as implants or as cell culture 3D devices for fundamental cellular studies.

Correspondence to: Hellen Altendorf, Department of Image Processing, Fraunhofer Institute of Industrial Mathematics, Fraunhofer-Platz 1, D-67663 Kaiserslautern, Germany, Centre of Mathematical Morphology, Mines Paris Tech, 35 rue Saint Honoré, 77305 Fontainebleau cedex, France; e-mail: Hellen.Altendorf@mines-paristech.fr

In that context, second harmonic generation (SHG) microscopy has been shown to provide highly contrasted 3D images of fibrillar collagen in unstained biological tissues (Campagnola *et al.*, 2002; Zipfel *et al.*, 2003a; Pena *et al.*, 2007; Strupler *et al.*, 2007, 2008; Sun *et al.*, 2008; Matteini *et al.*, 2009) and in engineered tissues (Raub *et al.*, 2008; Bayan *et al.*, 2009; Bowles *et al.*, 2010; Pena *et al.*, 2010). SHG is indeed a coherent multiphoton process that is specific for dense and aligned structures, such as fibrillar biopolymers (collagen fibrils, myosin thick filaments, microtubules, etc.). It exhibits intrinsic 3D resolution like other multiphoton microscopies and offers increased penetration in scattering tissues compared to confocal microscopy (Zipfel *et al.*, 2003b). Quantitative analysis of SHG images have been reported and aimed to quantify the density or porosity of the collagen fibrillar network and the directional distribution of the fibrils (Pena *et al.*, 2007, 2010; Strupler *et al.*, 2007, 2008; Raub *et al.*, 2008; Sun *et al.*, 2008; Bayan *et al.*, 2009; Matteini *et al.*, 2009; Bowles *et al.*, 2010). However, the proposed methods have been restricted to sequential processing of 2D images from 3D image stacks. The development of 3D quantification tools is desirable to take full advantage of the 3D capability of SHG microscopy and to access the 3D architecture of collagen fibrils at micrometer scale.

This paper presents a method, adapted from Altendorf & Jeulin (2009) and Altendorf (2011), for 3D quantification of SHG 3D images of collagen fibrils.

Several methods have been proposed in the literature to deal with fibre quantification in 3D images. The chord length transform (Sandau & Ohser, 2007) works on binary images of nearly straight fibres with a significant thickness. The orientation of a foreground point is defined as the one of a fixed number of directions, having the longest chord length. The approach of the Gaussian Orientation Space (Robb *et al.*, 2007; Wirjadi, 2009; Wirjadi *et al.*, 2009) works on both binary or grey-level images with fibres of nearly constant thickness. Oriented Gaussian filters are applied with a fixed number of directions and the local orientation in a voxel corresponds to the orientation with the highest filter response. Further approaches for orientation estimation in local windows include the inertia moments (Bigun & Granlund, 1987; Reuze *et al.*, 1993), quadrature filters (Granlund & Knutsson, 1995) and the Hessian Matrix (Frangi *et al.*, 1998; Tankyevych *et al.*, 2008). All three methods assume constant local radii of the objects and work on grey-level images. The first two methods can also be applied to binary images.

A classical tool for local radius estimation is the morphological granulometry, which has inspired recent tools, like the ultimate opening (Beucher, 2007). It considers the changes of grey values after morphological openings of increasing size: at each pixel, the estimated radius is the size of the opening which modifies the most the local pixel intensity. This approach can be applied to several types of objects with a minimal size, as the discretization effect is high on small

structuring elements. Unfortunately, it is not precise enough for thin fibres, as in the case of collagen fibrils.

In this paper, the advantages of the state-of-the-art methods are combined in an approach applicable to grey-level images, with low-computation time and high precision. To achieve such results, some hypotheses on the image quality and resolution, as well as on the fibre structure, are required. The approach assumes fibres with a nearly circular cross section and a minimal diameter of at least 3 pixels. It can be applied to binary images as well as grey-level images with high contrast. In the case of low contrasted or noisy images, prefiltering can be used to smooth the image and to enhance the contrast. Contrary to the Gaussian Orientation Space or the chord length transform, the proposed method can return any orientation on the unit sphere surface $S^2 = \{v \in \mathbb{R}^3, |v| = 1\}$. The stereological idea of this approach has the advantage of a lower computing time when compared to other approaches. Furthermore, in contrast to the Gaussian Orientation Space or the inertia moments, there are no restrictions on the variation of the fibre radius in different objects.

This approach was evaluated on SHG images of collagen concentrated matrices that were grown using various chemical conditions to adjust the size and density of the fibrils (Gobeaux *et al.*, 2008). The results include maps of the local features and the global distribution of orientation and radius, as well as a segmentation of the image into foreground and background, which yields a density estimate of the material. The foreground pixels are associated with the preferred orientations to visualize the spatial arrangement of the preferred orientations.

To the best of the authors' knowledge, this paper provides the first automated 3D image processing method dedicated to the quantification of SHG images on collagen samples.

The remainder of this paper is structured as follows: the whole process, including the preparation of the material, the nondestructive imaging technique and the analysis of the 3D fibrillar structure, is described in the 'Methods' section. In the 'Results' section, the method is evaluated on four samples. After discussing the methodology and the results, conclusions are drawn.

Methods

Fibrillar matrix preparation

Collagen I was purified from Wistar rat-tails tendon as previously described (Gobeaux *et al.*, 2007). Purity and homogeneity of the solution were verified by SDS-PAGE electrophoresis. Collagen I diluted solutions were then concentrated by centrifugation at 14 000 g using 3 kD filters tubes (VIVASPIN 20, Sartorius, Goettingen, Germany). These concentrated collagen solutions were checked for their hydroxyproline amount and adjusted to 100 mg mL⁻¹. The concentrated solutions were then deposited in Teflon

crucibles (3 mm wide, 5 mm long and 2 mm deep). The outer surface was gently flattened out longitudinally using a glass coverslip. Subsequently, the Teflon moulds were tightened into a dialysis membrane and dipped into a phosphate buffer saline (PBS) solution to induce the collagen fibrillogenesis and synthesize fibrillated matrices. On the basis of conditions already published (Gobeaux *et al.*, 2008), two different PBS concentrations were used to vary the size of the collagen fibrils: 50 and 100 mM, at pH = 7.4. After a few days, the collagen fibrillated matrices were taken off the moulds and were directly plunged into the buffer solutions and stored at 4°C until used.

Imaging

SHG imaging was performed using a custom-built multiphoton microscope as previously described (Pena *et al.*, 2007, 2010; Strupler *et al.*, 2007, 2008). Excitation was provided by a femtosecond Titanium-sapphire laser tuned at 730 or 860 nm. A quarter waveplate was used to achieve quasicircular polarization and mitigate the sensitivity of SHG images to the orientation of the fibrils in the focal plane. Excitation was focused in the fibrillar matrix using a water-immersion 20×, 0.95 NA objective. The lateral and axial resolutions near the sample surface were respectively 0.350 and 1.6 μm. Power at the sample was typically 10–30 mW. SHG signals were epidetected using photon-counting photomultiplier tubes and appropriate spectral filters. 3D images were obtained by laser scanning in the *xy* directions using galvanometric mirrors and moving the objective lens in the *z* direction. We used typically 100 kHz pixel rate and a sampling of 0.2 μm in *xy* direction and 0.5 μm in *z* direction. Images were saved as *z*-stacks of 2D grey-level images where the voxel values corresponded to the number of photons detected during the pixel dwell time.

Images were preprocessed to reduce noise and artefacts. A smoothing filter with a Gaussian kernel was used, followed by a linear spread of the grey values to enhance the contrast. The images were also cropped to remove distortion artefacts at the boundaries, because of the slight slowing down of the laser scanning while turning back.

Image analysis

In this section, we describe the image analysis approach designed to estimate local orientation and radius of fibrils based on directional distance transform, morphological gradient, and inertia moments. The approach works directly on 3D grey-level images and generates 3D orientation and radius maps, without any need for the extraction of individual fibres in the images. This extraction would be very difficult or even impossible to perform in the present case.

Overview of the method

Our approach starts with the directional distance transform to calculate, for every pixel of the image, the distance to a fibre boundary in 26 directions. The boundary coordinates are used to calculate the inertia moments from which the main inertia axes, giving the fibre orientation, are extracted. From the fibre orientation and the 26 directional distances the fibre radius can be estimated. Distributions are extracted from the orientation and radius maps in form of a histogram over all fibre points weighted with a quality measure.

The proposed approach is based on Altendorf & Jeulin (2009). The approach was slightly adapted with regard to the directional distance transform for grey-level images. In the case of the collagen fibrils, there is a high contrast between foreground and background and therefore a grey-level line can be completely classified into foreground and background regions. The approach in Altendorf & Jeulin (2009) was designed, more generally, for fibres of various grey-levels, where boundaries between fibres of different grey-levels need to be recognized as well. In the case of bright fibres on dark background, the adapted method yields more precise results for classification and measurement.

Working hypotheses for our approach are fibres with circular cross sections and a minimal diameter of 3 pixels.

Directional distance on grey level images

The thresholded quasi-distance used in Altendorf & Jeulin (2009) was replaced, in this study, by a so called maximal-mean-gradient approach, inspired by the morphological gradient. The input of this approach is a grey-level line $l : \{1, \dots, n\} \rightarrow \mathbb{R}$, which is extracted from a 3D image as an intensity profile along a specific direction. Zeros are added at the front and the back of the line and intermediate points are introduced with the average value of their two neighbours. This results in an upsampled line $l^2 : \{1, \dots, 2n + 3\} \rightarrow \mathbb{R}$, which is defined as follows:

$$l^2(i) = \begin{cases} l((i-1)/2) & \text{for } (i-1)/2 \in \{1, \dots, n\} \\ 0 & \text{for } i = 1 \text{ or } i = 2n + 3 \\ (l^2(i-1) + l^2(i+1))/2 & \text{else} \end{cases} \quad (1)$$

The gradient at point i with step size s is defined as $g(i, s) = l^2(i + s) - l^2(i - s)$. Note that this gradient can be positive or negative, respectively, if the grey values along the line increase or decrease. The classical morphological gradient corresponds to $|g(i, 1)|$. Along a grey-level line, the increase or decrease of the grey values depends highly on its angle with respect to the fibre orientation. If the line is perpendicular to the fibre, the grey-level change will be abrupt; with decreasing angle the grey value variation will protract over several pixels, thus $g(i, 1)$ will only detect a part of the gradient. To detect boundaries of grey-level slopes with different declines, gradients are averaged over various step sizes. This can

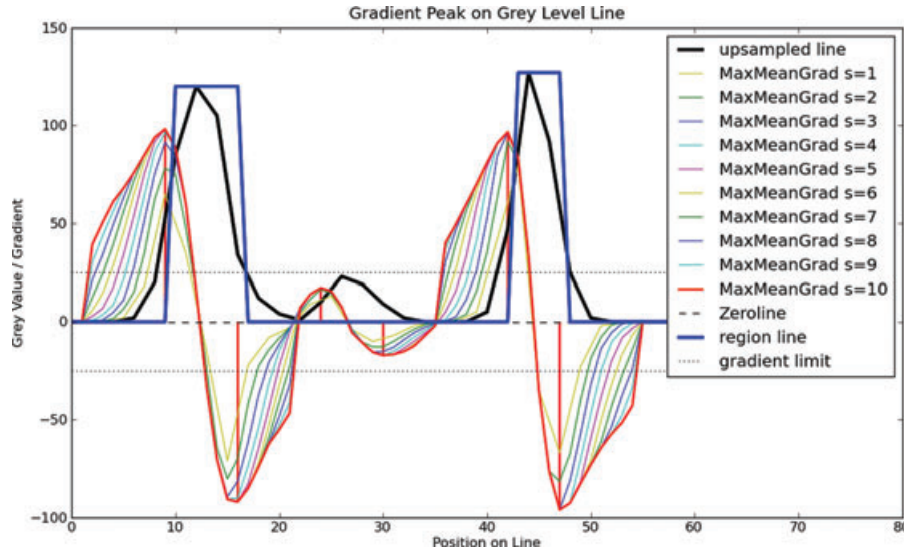


Fig. 1. Grey value line from a collagen image with maximal-mean-gradients, peak sequence and estimated boundaries.

also improve the robustness with respect to salt and pepper noise.

The mean gradient at a point i for the step size s is defined as

$$G_{\text{mean}}(i, s) = \frac{1}{s} \sum_{k=1}^s g(i, k). \quad (2)$$

If s is too large, peaks will diffuse and even merge with surrounding peaks. To keep high and localized peaks, we introduce the maximal-mean-gradient, which increases with the step size. To handle salt and pepper noise, a minimal step size s_0 is defined for the initial mean gradient. Then the maximal-mean-gradient is recursively defined as

$$G_{\text{mean}}^{\max}(i, s) = \begin{cases} G_{\text{mean}}(i, s) & \text{for } s \leq s_0 \\ G_{\text{mean}}(i, s) & \text{for } (s > s_0) \\ & \text{and } |G_{\text{mean}}(i, s)| > |G_{\text{mean}}^{\max}(i, s-1)| \\ & \text{and } (\text{sign}(G_{\text{mean}}(i, s)) = \text{sign}(G_{\text{mean}}^{\max}(i, s-1))) \\ G_{\text{mean}}^{\max}(i, s-1) & \text{else} \end{cases} \quad (3)$$

The meaningful extrema of $i \mapsto G_{\text{mean}}^{\max}(i, s)$, for a given s , are extracted in three steps. First, the extrema between two sign changes are considered and only the highest ones are kept. That gives us a sequence of peaks with alternating signs. Then peaks with an amplitude lower than a given gradient threshold G_0 are deleted, as they are not significant. This sequence is again reduced to an alternating one by extracting the extrema of neighbours with the same sign. The resulting sequence of peaks represents the significant fibre boundaries on the line and defines a foreground and background classification.

Figure 1 shows an example of an extracted line from one of the collagen images. The profile of the grey values is presented by the thick black line. The thin coloured lines represent the maximal-mean-gradient for different step sizes. The minimal

step size was chosen as $s_0 = 4$. The final maximal-mean-gradient for step size $s = 10$ is presented in red, with the first sequence of alternating peaks. The thick blue line represents the final estimated boundaries. The parameters $s_0 = 4$ and $s = 10$ are appropriate for various kinds of images and materials. The significant lower limit G_0 for the gradient depends on the contrast between the foreground and background in the original image. Therefore, it needs to be adapted according to the imaging technique and to the type of material. Approximately one quarter of the mean grey level contrast between the fibres and the matrix is a good guideline. This limit can be optimized by checking the classification map c , which contains optimally only two values 0 and 26. For the current application, the limit G_0 was set to 25.

Local orientation and radius estimation

Using the above described method, a given 3D grey-level image $f : I \rightarrow \mathbb{R}$ is scanned with 13 directional lines corresponding to the 26 neighbourhood. Maximal-mean-gradient values on the line indicate significant changes in the grey values, which represent boundaries of fibres. By recognizing the boundaries, we can define the directional distance in forward and backward directions for every voxel on the line. After testing all 13 directions, we get for every voxel and for 26 orientations, the information of the directional distance $d : I \times N_{26} \rightarrow \mathbb{R}^+$ to a fibre boundary and if the boundary indicates a transition from foreground to background or *vice versa*. The sum of the last mentioned information leads to a classification of the voxel in 27 classes $c : I \rightarrow \{0, \dots, 26\}$, which represents the number of directions, for which the voxel is classified as foreground. It is assumed that the analysis is meaningful, if the classification output is higher than a limit c_0 , which was set equal to 20 in this application. The thresholding of the classification map with the limit

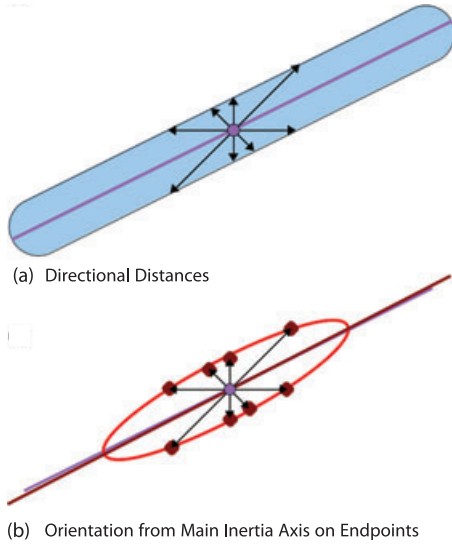


Fig. 2. 2D example of the orientation analysis from directional distances and inertia moments of boundary points. (a) shows a synthetic fibre in blue, an arbitrary point in the object in lilac and the directional distances as arrows in the sampled directions. (b) shows the point of interest with the directional distances $d(v_i)$ as black arrows and the extremities $e(i)$ as dark red points. The computation of the inertia moments can be interpreted as an ellipse fitting. The ellipse is shown in red with its main inertia axis (dark red line), that matches nearly perfectly the fibre orientation (lilac line). These illustrations are in 2D, but the process is done in 3D, with ellipsoids.

c_0 defines a mask for the foreground voxels. For c_0 close to 26, the foreground pixels mainly include bright pixels localized in the inner part of fibres, this generates a high specificity of the measure but shrinks the fibres shape within the segmented mask. It does not affect the radius estimate, as this one is based on the distances calculated from the grey-level images.

For an arbitrary pixel $i \in I$, the boundary points $e(i, v)$ are defined as points where the directed line reaches the first significant change: $e(i, v) = d(i, v) \times v$, where $v \in N_{26}$ and $d(i, v)$ is the distance to the next boundary in direction v . Inertia moments at point i are calculated on the set of boundary points $E(i) = \{e(i, v), v \in N_{26}\}$. For details on inertia moments see Duda & Hart (1973), Bakhadyrov & Jafari (1999) and McCartin (2007). Inertia moments of first degree return the centre of gravity $g(i)$. The main inertia axis provides an initial estimate of the local orientation of the fibre. The inertia axes and moments enable a rough fit of an ellipsoid to the structure of the boundary points (as shown in Fig. 2). The main inertia axis can have any orientation in S^2 and is not limited to the 26 sampling directions. Still, there is a bias towards the sampled directions. The correction of this bias is explained in Altendorf & Jeulin (2009). The notion of directional distances and the estimation of the main inertia axis are illustrated in Figure 2.

All calculations have been based so far on pixel information. For a nonisotropic pixels spacing $s = (s_x, s_y, s_z)^T$, as it is the

case in our application, a pixel-based orientation vector $v \in S^2$ is scaled as follows:

$$S(v, s) = \frac{V(v, s)}{L(v, s)} \quad \text{with } V(v, s) = \begin{pmatrix} v_x \cdot s_x \\ v_y \cdot s_y \\ v_z \cdot s_z \end{pmatrix} \quad (4)$$

$$\text{and } L(v, s) = |V(v, s)|$$

The final orientation $o(i)$ is obtained by scaling the deviation-corrected and pixel-based orientation $o'(i)$ with the spacing s : $o(i) = S(o'(i), s)$. The final orientation estimate is saved in the orientation map $o : I \rightarrow S^2$. The scaling needs to be applied after the deviation correction as the latest is developed for a sampling on the 26 adjacency system and would not work correctly on a deformed orientation vector.

With the knowledge of the fibre orientation, for every boundary point $e(i, v)$ we obtain an approximation of the radius of the fibre

$$r(i, v) = \frac{|e(i, v) - e(i, -v)|}{2} \sin(\angle(e(i, v) - e(i, -v), o(i))) \quad (5)$$

For a nonisotropic pixel spacing, distances need to be scaled with s and the radius estimate (with spacing) reads:

$$r(i, v) = \frac{L(e(i, v) - e(i, -v), s)}{2} \times \sin(\angle(S(e(i, v) - e(i, -v), s), o(i))) \quad (6)$$

Note that the radius estimate of Eq (6) is given in spacing units as s , whereas Eq (5) is based on pixels.

Let $r_{(1)}, \dots, r_{(26)}$ be the ordered sequence of those radius approximations. The final radius estimation is a trimmed mean of this sequence $r(i) = \frac{1}{8} \sum_{j=10}^{17} r_{(j)}$, which is saved in the radius map $r : I \rightarrow \mathbb{R}^+$. The trimmed mean discards outliers and is therefore more robust in terms of statistical analysis. Furthermore, the ratio of the first two inertia moments m_1, m_2 is saved in a ratio map $w : I \rightarrow [0, 1]$, where $w(i) = 2(\frac{m_2}{m_1+m_2} - 0.5) = \frac{m_2 - m_1}{m_1 + m_2}$. At each pixel, this ratio is an indicator for the elongation of the object defined by the boundary points. Therefore, the ratio of inertia moments as well as the classification of a voxel indicate the quality of the analysed orientation and radius. In particular, at fibre crossings, where the orientation and also the radius cannot be measured correctly, the moment ratio is low. A quality measure index $q : I \rightarrow \mathbb{R}^+$ is defined as the product of moment ratio and the label classification: $q(i) = w(i)c(i)$.

Border effects can be reduced by replacing the results on point i with those of the nearest image point to its gravity centre $g(i)$. This point is usually closer to the fibre core, where the directional distances and therefore also the measures are more stable.

Extraction of distributions

The radius distribution is represented by a weighted histogram with bin sizes h_w . The masked foreground voxels $I_m = \{i \in I, c(i) > c_0\}$ contribute to the histogram with a weight

Table 1. Data Set Information.

Index	Matrix		Surface material	Excitation		
	Collagen (mg mL ⁻¹)	PBS (mM)		Wavelength (nm)	Power (mW)	Image size [voxel]
I	100	50	Membrane	860	20	(581, 601, 60)
II	100	50	Membrane	730	30	(575, 601, 80)
III	100	50	Teflon	860	30	(801, 801, 70)
IV	100	100	Teflon edge	860	10	(700, 700, 65)

Note. The fibrillar collagen matrices were obtained from 100 mg mL⁻¹ collagen solutions that were fibrillated in 50 or 100 mM PBS to achieve two different ranges of fibril diameters (Gobeaux *et al.*, 2008). Different 3D regions of the matrices were imaged to study the effect of the surface interactions during the fibrillogenesis process (dialysis membrane, Teflon, Teflon edge). SHG imaging used either 860 or 730 nm laser excitation, with various excitation powers. Different image sizes were used, depending on the sample. The image sampling is 0.2 μm in the xy direction and 0.5 μm in the z direction.

of quality $q(i)$ divided by the approximated fibre cross section $\pi r(i)^2$. The division by the fibre cross section will change the volume-weighted distribution to a length-weighted distribution. This means that a fibre participates to the distribution according to its length instead of its volume. This step is important, as the volume is also dependent on the radius and therefore a volume-weighted radius distribution would be biased towards large fibres. The relative quantity of a histogram bin $b(k) = [(k-1)h_w, kh_w]$ is then defined as

$$H_r(k) = \frac{1}{W_r} \sum_{i \in I_m, r(i) \in b(k)} \frac{q(i)}{\pi r(i)^2} \quad (7)$$

where W_r is a normalizing factor, so that the integral over the whole histogram is equal to one: $\sum_{k=1}^{\infty} H_r(k) = 1$.

For the orientation distribution, a grid is projected on the unit sphere to partition the sphere surface in m cells $C_1, \dots, C_m \subset S^2$. Again, the masked foreground voxels contribute to the histogram with a weight set to their quality index, so the distribution is defined by

$$H_o(k) = \frac{1}{W_o} \sum_{i \in I_m, o(i) \in C_k} q(i) \quad (8)$$

where W_o is the normalizing factor, so that the integral over the distribution is equal to one. The orientation distribution is volume-weighted. If radius, length and orientation of a fibre are independent, the volume-weighted orientation distribution, as well as the length-weighted radius distribution, do not differ from their number-weighted versions (find a detailed discussion in the Appendix).

Results

Four collagen matrices (I–IV) were included in this study, generated by collagen dense solutions fibrillation in Teflon containers, via a dialysis against phosphate buffer solutions (50 mM: I–III or 100 mM: IV). SHG images revealed important variations of the organization and diameters of the fibrils as a function of the surface in contact with the collagen

solution during the fibrillogenesis. A dependence of the SHG fibrils diameters on the solvent used for the fibrillogenesis was also observed. This work aims to quantify these observations.

Table 1 describes the composition of the materials, indicates the size and resolution of the images and assigns an identifying index.

SHG images were analysed as described in the Methods section. A summary of the quantitative measures extracted from the analysis is provided in Table 2. The orientation distribution is described by histograms on a cell division of the unit sphere. The densities of the fibrils within the matrices, as well as their mean diameters and orientations, are reported for each sample. The main orientations given in the table correspond to the supporting vectors $u \in S^2$, $u = (u_x, u_y, u_z)^T$ of the three cells with the locally highest frequency.

Moreover, for every data set, a collection of images (illustrated in Figs 4–7) was created, including (a) volume rendering of the original grey-level image, (c) calculated orientation distribution and (f) diameter distribution. We also extracted the most frequent orientations and defined influence regions around them. These regions were labelled with colours (d). The choice and size of the classes were manually defined, thus their surface does not exactly correspond to the distribution density. This defined a labelling on the local orientations map, which can be projected on the surface rendering of the binarized classification image (b). Additionally, a colour-coded depth profile of the densities of the main orientations was created (e). The overall density is presented in black and the nonassigned pixels in grey.

Concerning the diameter distributions (Figs 4–7(f)), it should be stressed that the first classes (0.0–0.4 μm) are just within the lateral resolution of the microscope and probably correspond to the sharp extremities of the fibres.

Concerning the depth profile of the main orientations (Figs 4–7(e)), the curves of the main orientations follow mainly the trend of the total density for the images I–III. There is no significant change in the profile of the main orientations at

Table 2. Summary of Results.

Index	Density (%)	Mean diameter in μm ($\pm\text{SD}$)	Main orientations ($u_1, u_2, u_3 \in S^2$) (The three most frequent orientations)
I	4.61	1.08 (± 0.30)	(0.85, -0.07, -0.52) (-0.54, 0.54, 0.64) (-0.08, 0.97, 0.23)
II	3.43	0.96 (± 0.23)	(0.54, 0.54, 0.64) (0.54, -0.54, 0.64) (-0.54, -0.54, 0.64)
III	4.48	1.18 (± 0.55)	(0.08, 0.97, -0.23) (-0.08, 0.97, 0.23) (0.99, -0.08, 0.08)
IV	1.33	1.84 (± 0.43)	(0.23, 0.97, 0.08) (0.85, -0.52, 0.07) (0.75, 0.64, 0.18)

Note. The density derived from the foreground mask, the mean diameter as a trimmed mean ($\alpha = 5\%$) and the standard deviation from this value as well as the three main orientations, which are manually extracted from the histogram on the unit sphere. The collagen density and the main orientations vary with the imaging conditions (sample side, excitation power), whereas the mean diameter is quite reproducible for the same sample composition.

different depths. For image IV, the two peaks in the total density are essentially formed by the red curve, where the first peak is accentuated by the green curve. The other main orientations are uniformly distributed in depth.

Discussion

In this section, both the resulting data and the presented quantification method are discussed.

Comparison with manual fibre quantification

To validate this fibre quantification methodology, we compared our results with manual measurements, traditionally used to calculate the fibril diameter. The traditional manual fibril quantification was calculated on the cumulative projection of the 3D image on the xy plane. Several representative fibril sections were selected manually and a Gaussian Function was fitted to their grey value profile. The full width of the function at half of its maximum (FWHM) was supposed to indicate the diameter of the fibril. This measure is linearly dependent on the standard deviation

parameter σ of the Gauss function: $\text{FWHM}(\sigma) = 2\sigma\sqrt{2\ln 2}$. Table 3 shows the results of the manual FWHM method and the automatic quantification described in this paper on 8 test points in each image. It shows a systematic bias between manual and automatic measurements, while samples are sorted in the same way.

Figure 3 shows the perfect profile of the cumulative projection of a cylinder (a basic fibril model) and its Gaussian fit. We observe that the Gaussian model corresponding to the manual measure seems to underestimate the fibril diameter. In practice, regardless of the imaging technique, objects in 2D and 3D images are deformed because of the point spread function of the imaging system when their size is within the same order of magnitude as the microscope optical resolution, so that they tend to be fuzzy. This results in a projected curve which is closer to the Gaussian bell shape. However, it is not clear how to relate automatic and manual measures to the true fibril width. The FWHM method considers the width at the height of half the maximum as the object width. Figure 3 shows that this can result in an underestimation of the width with a factor of $f_0 = 0.586$, which can explain a systematic bias between the manual and automatic measurements. For the images I–

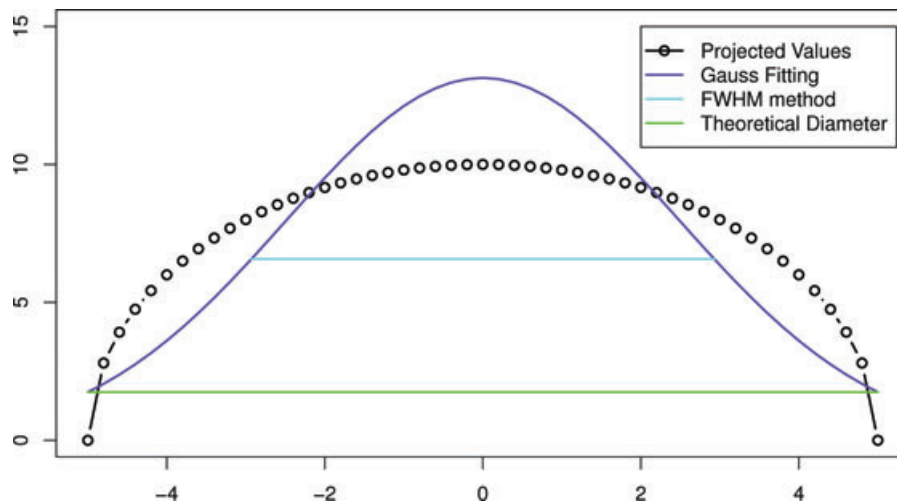


Fig. 3. Fitting of a general Gaussian curve to the profile of a projected fibril with circular cross section.

Table 3. Comparison of the Results from the Manual FWHM Method and the Automatic Quantification Described in this Paper on 8 Test Points in each Image.

Image index	FWHM mean diameter (μm)	Automatic mean diameter (μm)	Mean factor FWHM/automatic	Standard Deviation of the Factor
I	0.674	1.853	0.372	0.058 (15.64%)
II	0.581	1.236	0.480	0.098 (20.41%)
III	0.844	2.401	0.350	0.037 (10.60%)
IV	1.739	2.787	0.632	0.100 (15.81%)

III, we observe even smaller factors between the FWHM and our method (see Table 3). However, for image IV (which yields a higher fibril resolution), the factor is extremely close to the theoretical f_0 . That leads us to the assumption that the bias in the images I–III can be explained by the low resolution of the fibrils. Note furthermore, that on images II and IV, the deviation between the FWHM and our measurement multiplied with the factor f_0 is lower than the pixel sampling of $0.2 \mu\text{m}$.

Moreover, we need to exhibit a stable factor between the measures, to validate the automatic method with respect to the manual measurements. In our case, the variation of the factor within the same image (indicated by the standard deviation, column 5 in Table 3) is acceptable, whereas the variation of the factor between different images is significant. As mentioned above, the different solution concentrations and imaging conditions might explain this fact since fibrils with different diameters around the microscope resolution do not exhibit similar profiles in the images.

Finally, the ground truth is not known and thus an accurate validation is very hard to perform. Noteworthy, the automatic quantifications sort the samples in the same order as the manual measures. The larger mean diameter is obtained for sample IV, then for sample III, then for sample I and finally for sample II using the two methods. We therefore expect that the automatic quantification is a reliable measurement of the variation of fibril diameter. Furthermore, automatic quantification can be performed on a much larger sample than manual measures, which strongly limits bias because of small sampling. Such a bias is clearly demonstrated by the bad agreement between the mean diameters obtained by automatic quantification in the whole images (Table 2) and the ones obtained in the 8 test points (Table 3).

Discussion on the methodology

Advantages of the proposed approach, compared to other 3D fibre quantification methods, is the combination of the high precision of the results, the direct application on grey-level images and the ability to handle various fibre radii. Furthermore, the method computes both fibre orientation and radius and has low computational time

because of the stereological approach. Such precise results require good image quality and a sufficient resolution of the fibres, the analysis being limited to fibres with at least 3 pixels for their fibre diameters. These constraints are verified for SHG images, because SHG is a coherent nonlinear process that provides highly contrasted images compared to linear optical techniques (Deniset-Besseau *et al.*, 2010). Note that this method, developed for fibrils with a circular cross-section, could be extended to ribbon-like structures to study other biologically-relevant collagenous and noncollagenous structures.

This 3D quantification method, compared to usual SHG image processing, is capable of fully exploiting the 3D capability of SHG imaging by providing the 3D orientation field of the collagen fibrils. Fibril orientations within the focal plane are easily retrieved from 2D images, but the fibril's orientations out of the focal plane are more difficult to obtain. They can be estimated from 2D images using a polarization-resolved setup and making some assumptions about the collagen tensorial SHG response (Erikson *et al.*, 2007). However, this approach is not as robust and accurate as direct 3D image processing because of polarization artefacts in scattering tissues (Gusachenko *et al.*, 2010) and of ambiguous polarization responses as a function of the in-plane and out-of-plane angles (Erikson *et al.*, 2007). Moreover, the computing time for the present version of the software in C++ is around 15–20 minutes per image (on a standard Desktop PC) for a nonoptimized implementation.

Most interestingly, our method successfully sorts out fibrils with significant out of focal plane orientation. It shows that these fibrils exhibit a significant SHG signal while they are not excited parallel to their main axis. These results are in good agreement with previous papers bringing evidence that the collagen SHG response cannot be reduced to only one nonvanishing tensorial component $\chi_{zzz}^{(3)}$, like a rod-like system along the z axis (Stoller *et al.*, 2002; Plotnikov *et al.*, 2006; Deniset-Besseau *et al.*, 2009; Gusachenko *et al.*, 2010). The $\chi_{zxx}^{(3)}$ and $\chi_{xxz}^{(3)}$ components contribute significantly to the SHG response and enable the visualization of fibres with axial orientations, although fibrils lying within the focal plane exhibit a better contrast. Polarization engineering could further improve the visualization of fibrils with axial

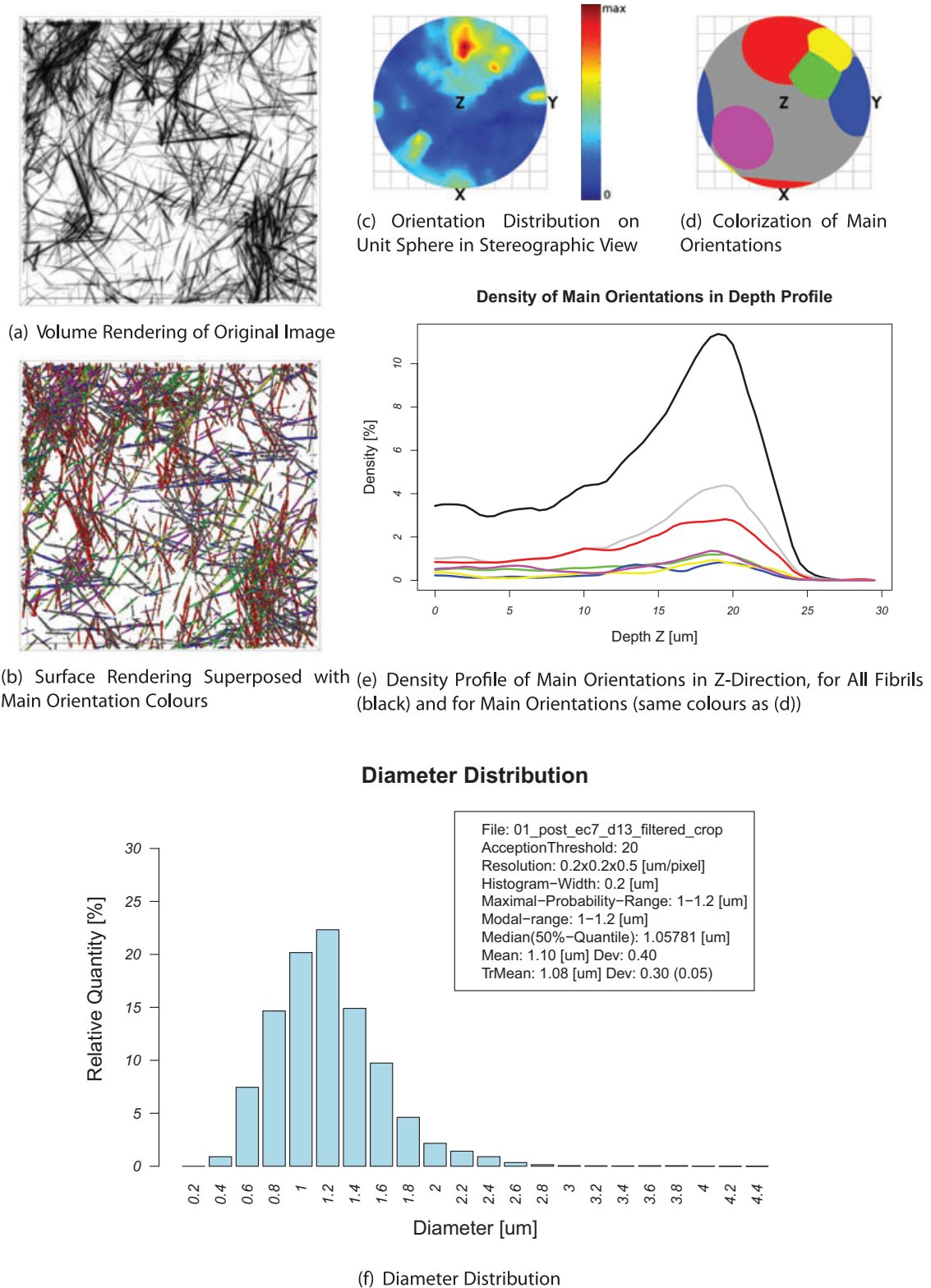
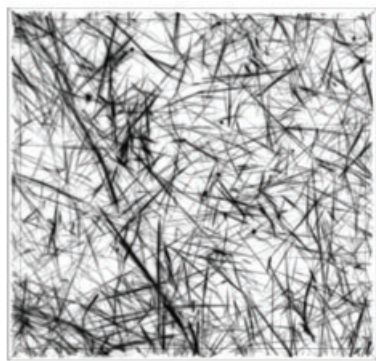
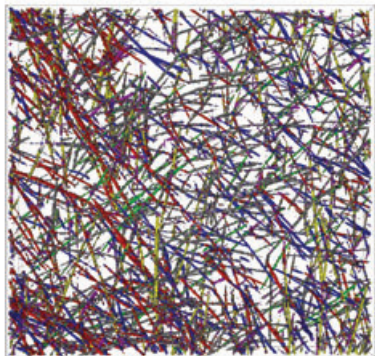


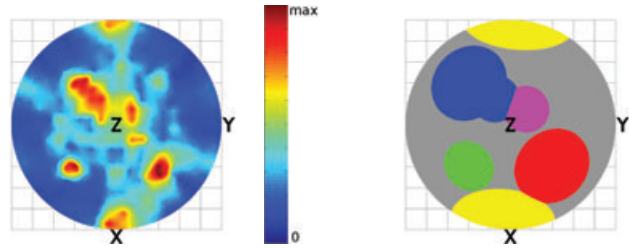
Fig. 4. Results for image I. 100 mg mL⁻¹ collagen in 50 mM phosphate buffer, imaged on the membrane side with 20 mW at 860 nm excitation.



(a) Volume Rendering of Original Image



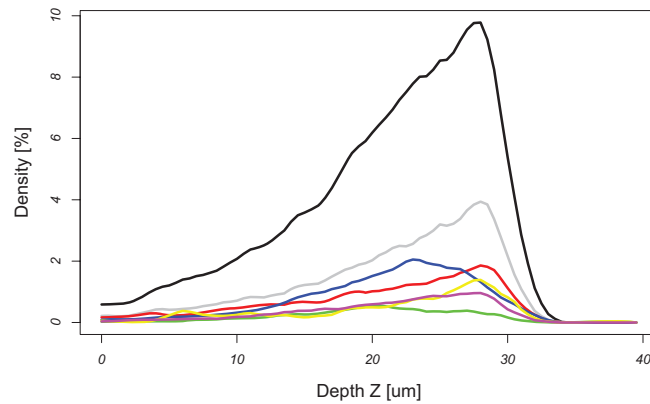
(b) Surface Rendering Superposed with Main Orientation Colours



(c) Orientation Distribution on Unit Sphere in Stereographic View

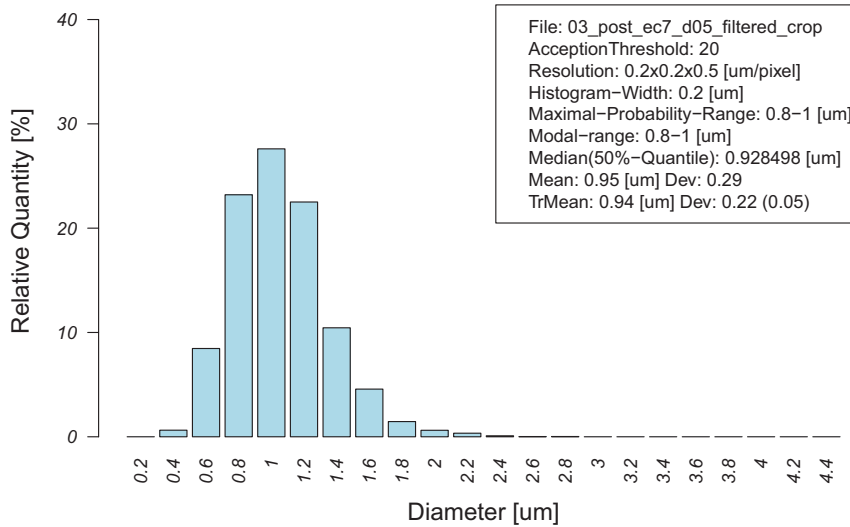
(d) Colorization of Main Orientations

Density of Main Orientations in Depth Profile



(e) Density Profile of Main Orientations in Z-Direction, for All Fibrils (black) and for Main Orientations (same colours as (d))

Diameter Distribution



(f) Diameter Distribution

Fig. 5. Results for image II. 100 mg mL⁻¹ collagen in 50 mM phosphate buffer, imaged on the membrane side with 30 mW at 730 nm excitation.

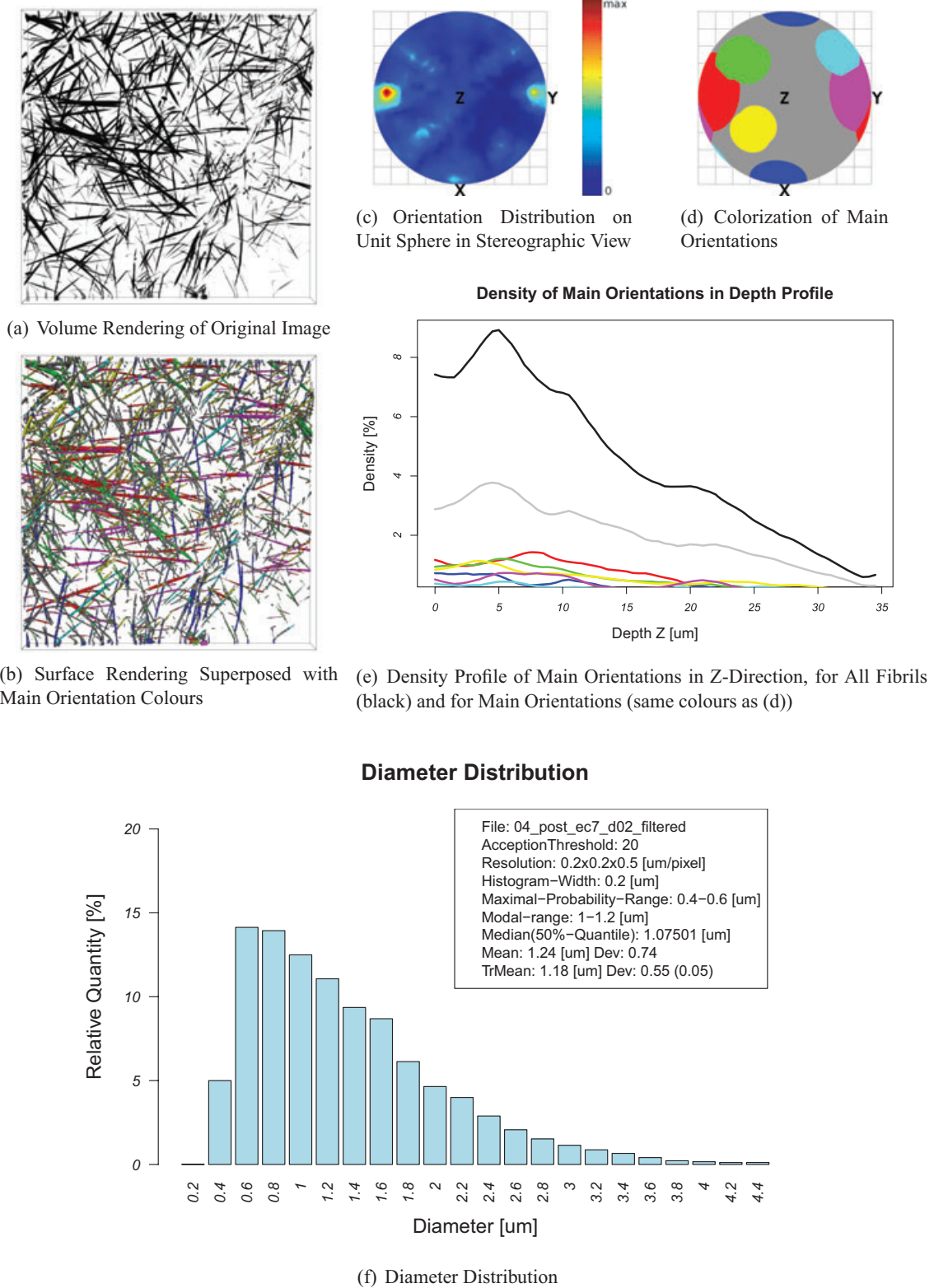


Fig. 6. Results for image III. 100 mg mL⁻¹ collagen in 50 mM phosphate buffer, imaged on the Teflon side with 30 mW at 860 nm excitation.

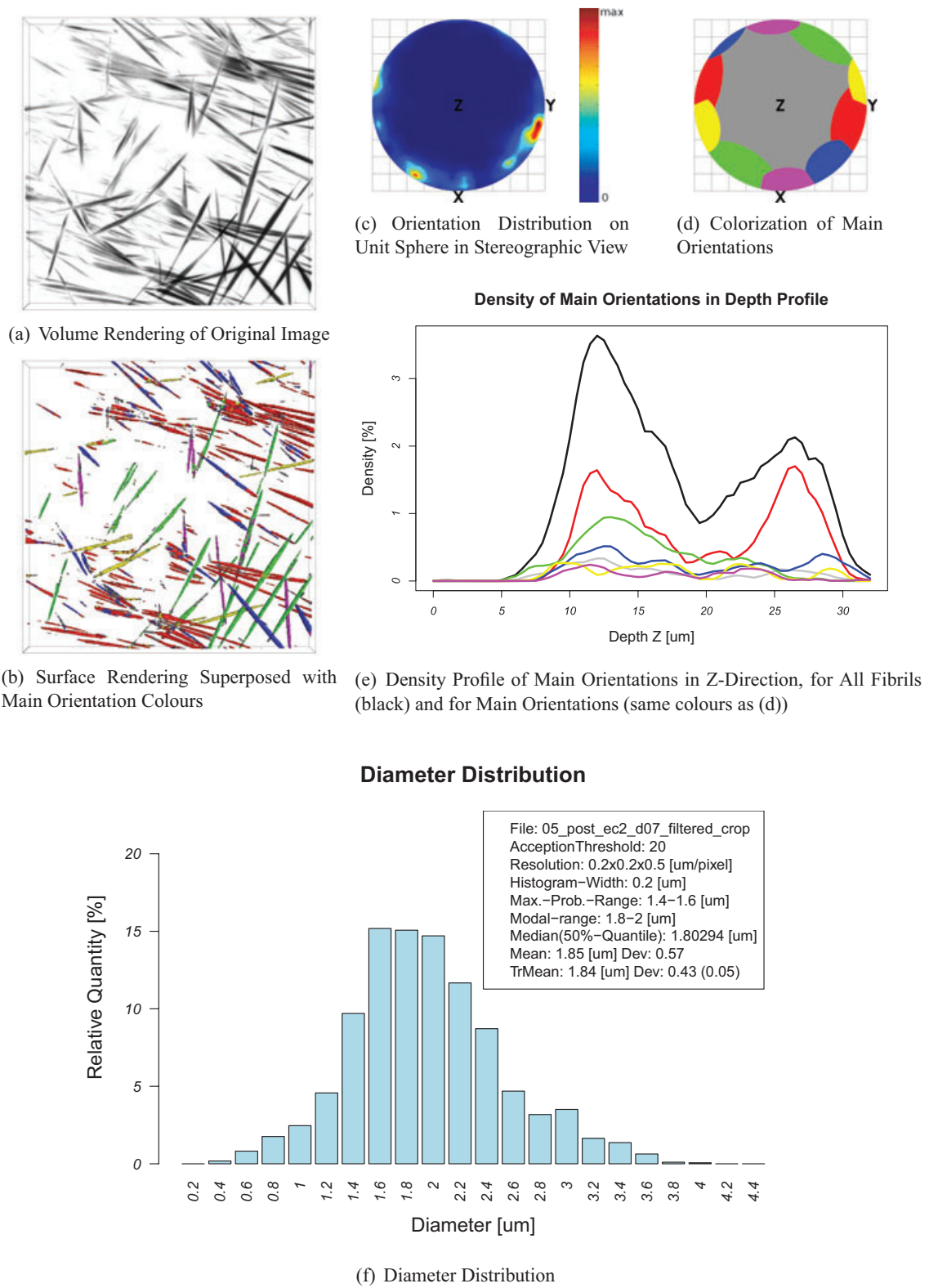


Fig. 7. Results for image IV. 100 mg mL⁻¹ collagen in 100 mM phosphate buffer, imaged at the edge of Teflon side with 10 mW at 860 nm excitation.

direction by providing axially polarized excitation fields (Yew & Sheppard, 2007; Yoshiki *et al.*, 2007). However, this technique has limited depth penetration in scattering collagenous tissues and would be restricted to thin samples or samples with low scattering, such as corneas.

Discussion on the quantification results

Retrieval of quantitative information from 3D SHG images is crucial to assess development of diseases or recoveries, as well as to guide the synthesis of collagen based scaffolds in the present context. To develop the appropriate analytical tools, 100 mg mL⁻¹ collagen solutions were used to generate dense collagen matrices. The solutions were fibrillated in specific buffer conditions (Na₂HPO₄, 50 and 100 mM) to generate two different fibril mean diameters and lengths. SHG images showed different fibrils dimensions and organizations of the inner part and the outer part of the scaffold. In the present data set, focus is on the outer crust of the scaffold, where fibrils are larger

Our image analysis method successfully discriminates between different fibrillar structures. As illustrated in Figure 4, the method is reliable even for dense and intricate matrices. A variation of the fibrils density with depth of the probed volume was observed in all data sets. The fibrils density first increases with the depth from 10 μm to 30 μm, which indicates a progressive increase in the scaffold density. The subsequent decrease, deeper in the scaffolds, is attributed both to a degradation of the imaging conditions because of scattering of the laser excitation and to a decrease in the fibrils diameter. Such variation of fibril diameter between the crust and the inner part was already observed by scanning electron microscopy on collagen matrices. These observations point out the importance of the surface interactions in the growing process of these matrices. All samples, however, exhibited similar density profiles for all main orientations. This shows that the anisotropy in the fibril 3D distribution does not change significantly with depth in the outer crust of the scaffolds for the first 30–40 μm depth.

Table 2 shows that the collagen density varies in images I–III, although they were measured in different regions of the same sample, with the same collagen and buffer concentrations. We attribute this discrepancy to differences in the imaging conditions. First, the excitation power varies from 10 to 30 mW and images acquired with lower excitation power may underestimate the collagen density. Second, the effective depth within the scaffold at $z = 0$ may differ from one image to the other, so that the scaffold is scanned in more or less dense areas. This means that only the relative variations of the fibrils density with depth can be considered as a reliable result, unless the imaging conditions are identical. On the contrary, the mean radii obtained in Table 2 are similar for images I–III. This shows that our method enables reliable quantitative measurements of fibril radii. Most interestingly,

it can be observed that the fibril mean radius at 100 mM phosphate buffer is roughly twice the one at 50 mM in similar conditions (i.e., a mean radius value of 1.07 μm for the three first samples and 1.84 μm for sample IV). The same behaviour was already observed in transmission electron microscopy measurements of the inner part of the matrix (Gobeaux *et al.*, 2008). This means that, although there is evidence of the significant effect of the surface interactions, the physico-chemical conditions of the fibrillogenesis solvent are still crucial. This point is critical, because synthesis of biomaterial for medical purposes will always, at some point, need some kind of patterning and shaping. The effect of the surface container should therefore always be checked and taken into account.

Conclusion

A direct 3D quantification method for collagen fibrillar networks in SHG images was presented. This approach enables quantifying the fibril density, orientations and radii within the collagen matrix. We compute also the average value, the standard deviation and the variation of these parameters along the depth within the scaffold. This image processing method fully exploits the 3D capability of SHG microscopy and makes this imaging technique a powerful tool for visualizing the 3D spatial distribution of collagen fibrils. This study focused on collagen scaffolds to gain some knowledge regarding collagen placement during the preparation of fibrillar matrices according to different subfields of the material. The differences observed between manual and automated image analyses are explained in the paper. The comparative analysis of the two methods enabled us to unambiguously link the two kinds of results for well defined experimental conditions. The proposed automatic measurements are therefore a reliable method to compare populations of collagen fibrils from images with similar acquisition conditions. Anyway, the automated image analysis based measurements can be performed on a much larger sample than manual counting. It also provides a variety of parameters that are not available using manual measures, such as 3D orientations of the fibrils.

The method can be readily extended to SHG images of other collagenous tissues. It could be used to study the cornea, which exhibits similar straight fibrillar structures and to the tendon or the dermis, because the approach also applies to crimped structures. The method could also be generalized to characterize collagen organization at different spatial scales. For instance, it could enable 3D quantification at nanometre scale of collagen molecules or molecular domains in collagen liquid crystals visualized by electron microscopy. Finally, the proposed approach is applicable to other fibrillar structures in various types of tissues, visualized by any other imaging technique with sufficient contrast. For instance, it may be applied to elastin fibres visualized by fluorescence confocal or multiphoton microscopy.

Acknowledgements

The authors thank Silvia Santos and Mathias Strupler for assistance during imaging experiments. A. Deniset-Besseau acknowledges the Fondation de la Recherche Médicale and P. De Sa Peixoto the Ecole Doctorale iViv and the UPMC for financial support. This work is also financially supported by the Institute Carnot M.I.N.E.S. and the Fraunhofer Institute ITWM, Kaiserslautern.

References

- Altendorf, H. (2011) *3D Morphological Analysis and Stochastic Modeling of Random Fiber Networks—applied on Glass Fiber Reinforced Composites*. PhD Thesis, Mines ParisTech, TU Kaiserslautern and Fraunhofer ITWM.
- Altendorf, H. & Jeulin, D. (2009) 3d directional mathematical morphology for analysis of fiber orientations. *Image Anal. Stereol.* **28**, 143–153.
- Bakhadyrov, I. & Jafari, M. (1999) Inertia tensor as a way of feature vector definition for one-dimensional signatures. *Proc. of ICSMC* **99**, 904–909.
- Bayan, C., Levitt, J.M., Miller, E., Kaplan, D. & Georgakoudi, I. (2009) Fully automated, quantitative, noninvasive assessment of collagen fiber content and organization in thick collagen gels. *J. Appl. Phys.* **105**, 102042-1-102042-11.
- Beucher, S. (2007) Numerical residues. *Image Vision Comput.* **25**, 405–415.
- Bigun, J. & Granlund, G.H. (1987) Optimal orientation detection of linear symmetry. *Proceedings of the ICCV*, London, U.K. IEEE Computer Society Press, pp. 433–438.
- Bowles, R.D., Williams, R.M., Zipfel, W.R. & Bonassar, L.J. (2010) Self-assembly of aligned tissue-engineered annulus fibrosus and intervertebral disc composite via collagen gel contraction. *Tissue Eng. A* **16**, 1339–1348.
- Brown, A.E.X. & Discher, D.E. (2009) Conformational changes and signaling review in cell and matrix physics. *Curr. Biol.* **19**, R781–R789.
- Campagnola, P.J., Millard, A.C., Terasaki, M., Hoppe, P.E., Malone, C.J. & Mohler, W. (2002) Three-dimensional high-resolution second-harmonic generation imaging of endogenous structural proteins in biological tissues. *Biophys. J.* **82**, 493–508.
- Deniset-Besseau, A., De Sa Peixoto, P., Mosser, G. & Schanne-Klein, M.-C. (2010) Nonlinear optical imaging of lyotropic cholesteric liquid crystals. *Opt. Express* **18**, 1113–1121.
- Deniset-Besseau, A., Duboisset, J., Benichou, E., Hache, F., Brevet, P.-F. & Schanne-Klein, M.-C. (2009) Measurement of the second order hyperpolarizability of the collagen triple helix and determination of its physical origin. *J. Phys. Chem. B* **113**, 13437–13445.
- Duda, R.O. & Hart, P.E. (1973) *Pattern Classification and Scene Analysis*. John Wiley & Sons Inc., New York.
- Erikson, A., Örtengren, J., Hompland, T., Davies, C.d.L. & Lindgren, M. (2007) Quantification of the second-order nonlinear susceptibility of collagen I using a laser scanning microscope. *J. Biomed. Optics* **12**, 044002-1-044002-10.
- Frangi, A., Niessen, W., Vincken, K. & Viergever, M. (1998) Multiscale vessel enhancement filtering. *Proceedings of the Med. Image Comput. Assist. Interv.* **98**, Berlin, Germany. Springer-Verlag, pp. 130–137.
- Gobeaux, F., Belamie, E., Mosser, G., Davidson, P., Panine, P. & Giraud-Guille, M.-M. (2007). Cooperative ordering of collagen triple helices in the dense state. *Langmuir* **23**, 6411–6417.
- Gobeaux, F., Mosser, G., Anglo, A., Panine, P., Davidson, P., Giraud-Guille, M.-M. & Belamie, E. (2008) Fibrillogenesis in dense collagen solutions: a physicochemical study. *J. Mol. Biol.* **376**, 1509–1522.
- Granlund, G.H. & Knutsson, H. (1995) *Signal Processing for Computer Vision*. Kluwer Academic Publishers, Dordrecht, the Netherlands.
- Gusachenko, I., Latour, G. & Schanne-Klein, M.-C. (2010) Polarization-resolved second harmonic microscopy in anisotropic thick tissues. *Opt. Express* **18**, 19339–19352.
- Hulmes, D. (2002) Building collagen molecules, fibrils, and suprafibrillar structures. *J. Struct. Biol.* **137**, 2–10.
- Lee, J., Cuddihy, M.J. & Kotov, N.A. (2008). Three-dimensional cell culture matrices: state of the art. *Tissue Eng. Part B* **14**, 61–86.
- Matteini, P., Ratto, F., Rossi, F., Cicchi, R., Stringari, C., Kapsokalyvas, D., Pavone, F.S. & Pini, R. (2009) Photothermally-induced disordered patterns of corneal collagen revealed by shg imaging. *Opt. Express* **17**, 4868–4878.
- McCartin, B.J. (2007) On concentration and inertia ellipsoids. *Appl. Math. Sci.* **1**, 1–11.
- Pena, A.-M., Fabre, A., Débarre, D., Marchal-Somme, J., Crestani, B., Martin, J.-L., Beaurepaire, E. & Schanne-Klein, M.-C. (2007) Three-dimensional investigation and scoring of extracellular matrix remodeling during lung fibrosis using multiphoton microscopy. *Microsc. Res. Tech.* **70**, 162–170.
- Pena, A.-M., Fagot, D., Olive, C., et al. (2010). Multiphoton microscopy of engineered dermal substitutes: assessment of 3d collagen matrix remodeling induced by fibroblasts contraction. *J. Biomed. Opt.*, **15** 056018-1-056018-7.
- Plotnikov, S.V., Millard, A., Campagnola, P. & Mohler, W. (2006) Characterization of the myosin-based source for second-harmonic generation from muscle sarcomeres. *Biophys. J.* **90**, 328–339.
- Raub, C.B., Unruh, J., Suresh, V., Krasieva, T., Lindmo, T., Gratton, E., Tromberg, B.J. & George, S.C. (2008) Image correlation spectroscopy of multiphoton images correlates with collagen mechanical properties. *Biophys. J.* **94**, 2361–2373.
- Reuze, P., Coatrieux, J., Luo, L. & Dillenseger, J. (1993) A 3d moment based approach for blood vessel detection and quantification in MRA. *Technol. Health Care* **1**, 181–188.
- Robb, K., Wirjadi, O. & Schladitz, K. (2007) Fiber orientation estimation from 3D image data: practical algorithms, visualization, and interpretation. *Proceedings of the HIS 07*, Kaiserslautern, Germany, pp. 320–325.
- Sandau, K. & Ohser, J. (2007) The chord length transform and the segmentation of crossing fibres. *J. Microscopy* **226**, 43–53.
- Stoller, P., Reiser, K., Celliers, P. & Rubenchik, A. (2002) Polarization-modulated second harmonic generation in collagen. *Biophys. J.* **82**, 3330–3342.
- Strupler, M., Hernest, M., Fligny, C., Martin, J.-L., Tharaux, P.-L. & Schanne-Klein, M.-C. (2008) Second harmonic microscopy to quantify renal interstitial fibrosis and arterial remodeling. *J. Biomed. Optics* **13**, 054041-1-054041-10.
- Strupler, M., Pena, A.-M., Hernest, M., Tharaux, P.-L., Martin, J.-L., Beaurepaire, E. & Schanne-Klein, M.-C. (2007) Second harmonic imaging and scoring of collagen in fibrotic tissues. *Opt. Express* **15**, 4054–4065.

- Sun, W.X., Chang, S., Tai, D.C.S., Tan, N., Xiao, G.F., Tang, H.H. & Yu, H. (2008) Nonlinear optical microscopy: use of second harmonic generation and two-photon microscopy for automated quantitative liver fibrosis studies. *J. Biomed. Optics* **13**, 064010-1-064010-7.
- Tankyevych, O., Talbot, H. & Dokladal, P. (2008). Curvilinear morpho-hessian filter. *Proceedings of the IEEE Int. Symp. Biom. Imaging 08 Paris, France*, pp. 1011–1014.
- Wirjadi, O. (2009) *Models and Algorithms for Image-Based Analysis of Microstructures*. PhD thesis, Technische Universität Kaiserslautern.
- Wirjadi, O., Schladitz, K., Rack, A. & Breuel, T. (2009) Applications of anisotropic image filters for computing 2d and 3d-fiber orientations. *Proceedings of the ECS 09, Milan, Italy. ESCULAPIO Pub. Co.*, pp. 107–112.
- Yew, E.Y.S. & Sheppard, C.J.R. (2007) Second harmonic generation polarization microscopy with tightly focused linearly and radially polarized beams. *Opt. Commun.* **275**, 453–457.
- Yoshiki, K., Ryosuke, K., Hashimoto, M., Araki, T. & Hashimoto, N. (2007) Second-harmonic-generation microscope using eight-segment polarization-mode converter to observe three-dimensional molecular orientation. *Opt. Lett.* **32**, 1680–1682.
- Zipfel, W.R., Williams, R., Christie, R., Nikitin, A., Hyman, B. & Webb, W. (2003a) Live tissue intrinsic emission microscopy using multiphoton-excited native fluorescence and second harmonic generation. *Proc. Natl. Acad. Sci. USA* **100**, 7075–7080.
- Zipfel, W.R., Williams, R. & Webb, W. (2003b) Nonlinear magic: multiphoton microscopy in the biosciences. *Nature Biotech.* **21**, 1369–1377.

Appendix

We consider a population of fibres with random radius R , length L and orientation Ω . The number and volume weighted multivariate distributions $f(r, l, \omega)$ and $g(r, l, \omega)$ are related as follows:

$$g(r, l, \omega) = k_1 r^2 l f(r, l, \omega) \quad (9)$$

with a normalization constant k_1 given by

$$k_1 = \frac{1}{\iiint r^2 l f(r, l, \omega) dr dl d\omega} \quad (10)$$

The marginal distributions of the orientation $f(\omega)$ and $g(\omega)$ are related by the following expression, deduced from Eq (9) :

$$g(\omega) = k_1 \iint r^2 l f(r, l, \omega) dr dl \quad (11)$$

If, for each fibre, the orientation is statistically independent of the radius and of the length, we have the decomposition

$$f(r, l, \omega) = f(\omega) f(r, l) \quad (12)$$

and

$$g(\omega) = f(\omega) k_1 \iint r^2 l f(r, l) dr dl = f(\omega) \quad (13)$$

as

$$\begin{aligned} k_1^{-1} &= \iiint r^2 l f(r, l) f(\omega) dr dl d\omega \\ &= \iint r^2 l f(r, l) \left(\int f(\omega) d\omega \right) dl dr. \end{aligned} \quad (14)$$

Per definition $f(\omega)$ is normalized, thus $\int f(\omega) d\omega = 1$. It follows

$$k_1^{-1} = \iint r^2 l f(r, l) dl dr \quad (15)$$

which eliminates the second constant in Eq. (13). Therefore, the assumption of independence involves that the volume and number-weighted distributions are the same. This result is true, even if the length and the radius of fibres are not independent.

Similarly, we can derive a relationship between the length ($h(r, l)$) and number ($f(r, l)$) weighted joint distributions of the random radius R with the random length L . We have

$$\begin{aligned} h(r, l) &= k_3 \int l f(r, l, \omega) d\omega \\ &= k_3 l \int f(r, l, \omega) d\omega = k_3 l f(r, l) \end{aligned} \quad (16)$$

with

$$k_3 = \frac{1}{\iint l f(r, l) dl dr} \quad (17)$$

When the random length L is independent of the radius R , we have the decomposition

$$f(r, l) = f(l) f(r) \quad (18)$$

and therefore $k_3 = \frac{1}{\int_0^\infty l f(l) dl} = \frac{1}{E[L]}$, with $E[L]$ being the number weighted average of the lengths of fibres. The marginal radius distribution becomes

$$\begin{aligned} h(r) &= k_3 \int_0^\infty h(r, l) dl \\ &= f(r) k_3 \int_0^\infty l f(l) dl = k_3 E[L] f(r) = f(r). \end{aligned} \quad (19)$$

Thus, the length and number weighted joint distributions of the random radius R are the same. This result is true, even if the radius and length are not independent of the orientation of fibres.